Assessment of a clinically feasible Bayesian fitting algorithm using a simplified description of Chemical Exchange Saturation Transfer (CEST) Imaging

Aaron Kujawa[a], Mina Kim[a], Eleni Demetriou[a], Annasofia Anemone[b], Dario Livio Longo[c], Moritz Zaiss[d], and Xavier Golay[a]

[a]Brain Repair and Rehabilitation, University College London, 8-11 Queen Square, London, WC1N 3AR, United Kingdom

[b]Molecular Biotechnology and Health Sciences, University of Torino, Via Nizza 52, 10126, Turin, Italy

[c]Institute of Biostructures and Bioimaging (IBB), National Research Council of Italy (CNR), Via Nizza 52, 10126 Torino~~,~~ Italy

[d]Magnetic Resonance Center, Max-Planck Institute for Biological Cybernetics, Max-Planck-Ring 8-14, 72076 Tübingen, Germany

Corresponding author.
Aaron Kujawa
aaron.kujawa.10@ucl.ac.uk

Abstract

Fitting a model based on the Bloch-McConnell (BM) equations to Chemical Exchange Saturation Transfer (CEST) spectra allows for the quantification of metabolite concentration and exchange rate as well as simultaneous correction of field inhomogeneity, direct water saturation and magnetization transfer. Employing a Bayesian fitting approach permits the integration of prior information into the analysis to incorporate expected parameter distributions and to prevent over-fitting. However, the analysis can be time consuming if a general numerical solution of the BM equations is applied. In this study, we combined a Bayesian fitting algorithm with approximate analytical solutions of the BM equations to achieve feasible computational times. To evaluate the accuracy and speed of the suggested approach, phantoms including Iodipamide, Taurine and Creatine were tested in addition to simulated data with continuous-wave (CW) and pulsed saturation with Gaussian pulses. A significant reduction of computational time was achieved when fitting CW data (about 50-fold) and pulsed saturation data (more than 100-fold) with the analytical model while the estimated parameters were largely consistent with the parameters from the general numerical solution. The increased speed of the algorithm facilitates the Bayesian analysis of CEST data within clinically feasible processing times. Other analytical models valid for different parameter regimes may be employed to extend the applicability to a wider range of CEST agents.

1. Introduction

Chemical Exchange Saturation Transfer (CEST) is an approach in magnetic resonance imaging (MRI) aiming to detect molecules containing exchangeable protons. The CEST contrast results from the selective saturation of these protons and their subsequent exchange with bulk water protons which in turn leads to a measurable reduction of the water signal. This CEST effect can be several orders of magnitude larger than the direct signal from the metabolites as measured with magnetic resonance spectroscopy (MRS) techniques, leading to enhanced sensitivity [1]. Various endogenous as well as exogenous CEST agents have been utilized in studies to investigate physiological parameters that are used as risk factors for the prediction of several pathologies[2–4]. For example, the endogenous CEST effect in Amide Proton Transfer (APT) imaging depends on the exchange rate of amide NH groups, which has been shown to be pH-dependent and capable of detecting pH deficits in stroke [5].

Several approaches have been adopted to quantify the CEST effect, such as, among others, the magnetization transfer ratio (MTR), the asymmetry magnetization transfer ratio (MTR_{asym}), quantitative CEST (qCEST) [6], the Omega plot [7], QUEST and QUESP (quantifying exchange rates using the saturation time and saturation power dependencies) [8] and QUEST with ratiometric analysis (QUESTRA) [9]. In the case of MTR, the water proton signal S_{sat} which is obtained upon saturation at a single offset frequency is compared to the water signal without saturation S_0. However, MTR might be overestimated due a direct effect on the water signal known as the “spill-over effect”. This effect is often symmetric with respect to the water frequency and can therefore be eliminated by means of an additional reference measurement at the negative offset frequency, which is exploited for MTR_{asym}. A bias is introduced, however, if the reference measurement is influenced by non-symmetric effects caused by exchanging protons with overlapping resonance frequencies or slow exchange processes mediated via the Nuclear Overhauser Effect (NOE) [10]. Furthermore, these metrics quantify the magnitude of the CEST effect, but do not give much insight about the underlying parameters such as agent concentration or exchange rate. These parameters can be determined by qCEST, Omega plot, QUEST, QUESP and QUESTRA. In contrast to MTR and $\mathrm{MTR}_{\mathrm{asym}}$, many acquisitions with varying saturation parameters (i.e. variations of the length and/or amplitude of the saturation pulse) are typically required which can result in long scanning times.

CESTR* is another metric that has recently been developed [11] and which has potential to quantify pH differences between tumour and normal tissue *in vivo* without the need for exogenous contrast agents [12]. This metric is calculated based on parameters estimated by a Bayesian model-fitting method [13], which has previously been shown to permit the quantification of the APT effect *in vivo*, even in the presence of asymmetries in the Z-spectrum arising from Magnetization Transfer (MT) or NOE-mediated contributions [11].

In contrast to conventional least-squares fitting [14,15], Bayesian model-fitting of the Z-spectrum provides a framework to combine *prior* information about the model parameters with the information inferred from the measured data, also referred to as the *likelihood*. The prior information reflects the expected values and uncertainties for each model parameter such as information available from previous experiments. Furthermore, this approach reduces the risk of over fitting which can arise when a large number of model parameters is estimated from fitting data with a low signal-to-noise ratio (SNR).

One of the main limitations of the current Bayesian model-fitting approach for CEST is the long processing time which can be up to several hours per acquired section [11]. Especially in the clinic such long processing times are not feasible. The bottleneck of the algorithm is the evaluation of the model itself which is based on a numerical solution of the Bloch-McConnell (BM) equations [16,17].

On the other hand, analytical approximations of the BM equations which were shown to be valid for different ranges of physiological parameter values and experimental settings have been developed [8,18–22]. Here, we show that the processing time of the Bayesian model-fitting approach can be reduced considerably by replacing the BM equations with analytical approximations without significantly affecting the resulting parameter distributions or the convergence of the algorithm. We evaluated the modified algorithm by comparing the estimated parameters to those obtained from the algorithm based on the numerical solution of the BM equations. This evaluation was performed on both simulated data and data from the measurement of phantoms. The analytical approximations that were applied in this study were derived by Zaiss et al. [23] for CEST data acquired with continuous-wave (CW) saturation and by Roeloffs et al. [21] for CEST data acquired with a pulsed saturation scheme. In the case of pulsed saturation, the analytical solution was further developed to be applicable to adiabatic Gaussian-shaped pulses.

2. Theory

Bayes theorem

Bayesian model-fitting is based on Bayes theorem which combines the prior distribution $p(\Theta)$ with the likelihood $p(S|\Theta)$ to obtain the posterior distribution $p(\Theta|\mathrm{S})$:

$$p(\Theta|\mathrm{S}) \propto p(S|\Theta)p(\Theta). \tag{1}$$

The measured data is given by S and the set of N model parameters by $\Theta = \{\Theta_1, \dots, \Theta_\mathrm{i}, \dots, \Theta_\mathrm{N}\}$. Assuming a model $f(\Theta)$ and additive Gaussian noise with standard deviation σ_n, the likelihood can be expressed by the probability density function:

$$p(S|\Theta) = \frac{1}{\sigma_n\sqrt{2\pi}} e^{\frac{(S-f(\Theta))^2}{2\sigma_n^2}}. \tag{2}$$

In the context of CEST, S represents one or multiple measured Z-spectra and Θ corresponds to the set of model parameters to be estimated by the fitting algorithm such as exchange rates and equilibrium magnetizations. Furthermore, the model is given by a numerical or, as applied in this study, analytical solution of the BM equations.

Integrating the posterior distribution over all model parameters but one, Θ_i, renders the so-called marginalized posterior $p(\Theta_\mathrm{i}|S)$ which reflects the estimated probability distribution for Θ_i. The mean of this distribution $\overline{p(\Theta_\mathrm{i}|S)}$ can be interpreted as the expected value of Θ_i and credible intervals can be determined, e.g. the σ-credible interval corresponds to the range of values within which Θ_i falls with a probability of 0.68.

A Z-spectrum can be accurately described by a model $f(\Theta)$ which is based on the BM equations. In this model, bulk water is described by pool a and the CEST agents are described by pools $i = b, c, d, \dots$. Each pool is modelled by its longitudinal and transverse relaxation rates T_{1i} and T_{2i}, equilibrium magnetization M_{0i}, resonance frequency ω_i and forward proton exchange rate constants k_{ij} with the other pools j. A general numerical solution of the BM equations can be found in [24], however its evaluation is computationally demanding as it contains a matrix exponential [15]. Instead of the full model, two simplified approximations for the cases of CW saturation and pulsed saturation were applied here.

CW saturation

For CW saturation, the following approximate solution for the normalized water pool magnetization in the direction of the main magnetic field $Z(t) = \frac{M_{za}(t)}{M_{0a}}$ was used [23]:

$$Z(t) = (P_z P_{zeff} - Z_{\mathrm{CW}}^{\mathrm{SS}}) \exp(-\mathrm{R}_{1\rho} t) + Z_{\mathrm{CW}}^{\mathrm{SS}}. \tag{3}$$

The parameter t represents the duration of the CW saturation. P_z and P_{zeff} are factors describing the projection of magnetization along the z-axis onto the direction of the effective magnetic field and vice versa. They are given by $P_z = P_{zeff} = \cos(\theta)$, where $\theta = \tan^{-1}\left(\frac{\omega_1}{\Delta\omega}\right)$ is the angle between the effective magnetic field and the z-axis. The parameters ω_1 and $\Delta\omega = \omega_{rf} - \omega_a$ designate the CW saturation amplitude and frequency offset with respect to the resonance frequency of the water pool. The steady-state value is given by

$$Z_{\mathrm{CW}}^{\mathrm{SS}} = \cos^2(\theta) \frac{R_{1a}}{R_{1\rho}}, \tag{4}$$

and the longitudinal relaxation rate of the water pool in the rotating frame, including the contribution due to chemical exchange, by $R_{1\rho}$. An approximate analytical expression for $R_{1\rho}$ for the case of multiple CEST pools is given in Appendix A.

Pulsed saturation

For pulsed saturation, we employ a solution termed ISAR2 derived in [21] for a series of n rectangular pulses of duration t_p, interleaved with delays of duration t_d and for 2 pools, i.e. the water and the CEST pool. This model assumes that the temporal evolution of the Z-spectrum is determined by an exponential decay with rate $R_{1\rho}$ during the rectangular pulse (according to equation 3), and by the biexponential dynamics of the free BM-equations during the inter-pulse delay. To extend the model for multiple CEST agent pools, we assume that $R_{1\rho}$ comprises the sum of contributions from each CEST pool to the exchange-dependent relaxation rate $R_{ex} = \sum_i R_{ex,i}$ (Appendix A). During the inter-pulse delay, we assume the N-exponential dynamics of the free BM-equations, where N is the number of modelled pools. The derivation as outlined in Appendix B is analogous to the derivation of the 2-pool model and leads to the following model for the Z-spectrum:

$$Z(n) = (Z_{\mathrm{I}} - Z_{\mathrm{pulsed}}^{\mathrm{SS}})\beta^n e^{-R_{1\rho} t_p n} + Z_{\mathrm{pulsed}}^{\mathrm{SS}}, \tag{5}$$

where Z_{I} is the initial normalized water magnetization.

Furthermore:

$$\beta = P_{zeff} P_{\mathrm{z}} \left(d_{aa} + \sum_i d_{ai} \Psi_i \right) \tag{6}$$

and

$$Z_{\mathrm{pulsed}}^{\mathrm{SS}} = \frac{P_{\mathrm{z}} P_{zeff} (1 - d_{aa} - \sum_i f_i d_{ai}) \exp(-R_{1\rho} t_p) + Z_{\mathrm{CW}}^{\mathrm{SS}} (1 - \exp(-R_{1\rho} t_p))}{1 - P_{\mathrm{z}} P_{zeff} (d_{aa} + \sum_i d_{ai} \Psi_i) \exp(-R_{1\rho} t_p)}. \tag{7}$$

The parameters Ψ_i represent the ratios of z-magnetizations of pools i and a at the end of the rectangular saturation pulse and can be approximated in the large-shift limit as:

$$\Psi_i = \frac{M_{zi}(t = t_p)}{M_{za}(t = t_p)} = f_i (1 - \alpha_{lab,i}), \tag{8}$$

where $\alpha_{lab,i}$ is the labelling efficiency of pool i:

$$\alpha_{lab,i}(\Delta\omega) = \frac{R_{ex,i}(\Delta\omega)}{f_i k_{ia}}, \tag{9}$$

The functions d_{aa} and d_{ai} represent the N-exponential decay of the magnetization during the inter-pulse delay. However, full expressions for these functions are very long. Thus, in analogy to the approximation given in Appendix D of [21] for $k_{ba} \gg R_{1a}$, we approximate these expressions by neglecting the quickly decaying exponential components for $k_{ia} \gg R_{1a}$ using the following simplifications of equations 6 and 7:

$$\beta = P_{zeff} P_z \exp(-R_{1a} t_d)(1 - \sum_i \alpha_{lab,i} f_i) \tag{10}$$

and

$$Z_{\text{pulsed}}^{\text{SS}} = \frac{P_z P_{zeff}(1 - \exp(-R_{1a} t_d)) \exp(-R_{1\rho} t_p) + Z_{\text{CW}}^{\text{SS}}(1 - \exp(-R_{1\rho} t_p))}{1 - P_z P_{zeff} \exp(-R_{1a} t_d)(1 - \sum_i \alpha_{lab,i} f_i) \exp(-R_{1\rho} t_p)}. \tag{11}$$

Extension to Gaussian-shaped pulses

Equation 5 was derived for a train of rectangular pulses. In the following, we assume that shaped pulses can be treated in a similar manner as the integration of adiabatic spin-lock pulses [25,26]. To extend the ISAR2 approach for shaped pulses, reasonable assumptions for the parameters P_z and P_{zeff} , the effective $R_{1\rho}$ and the initial relative pool magnetizations after the pulse given by Ψ_i have to be found.

1. Assumption: Shaped pulses are adiabatic. This is given if [27]: $\dot{\theta} \ll \omega_{eff}$. This allows the assumption $P_z = P_{zeff} = 1$.

2. Assumption: The effective $R_{1\rho}$ decay during the pulse can be described by the mean value $\overline{R_{1\rho}}$ given by:

$$\overline{R_{1\rho}} = \frac{1}{t_p} \int_{t=0}^{t_p} R_{1\rho}(\omega_1(t)) dt\,. \tag{12}$$

3. Assumption: The parameters Ψ_i represent the ratio of magnetizations of pool i and a at the end of the pulse and are given by equation 8 when rectangular pulses are considered. However, if the envelope of the RF pulse varies slowly with respect to k_i, the magnetization of pool i is determined by the last B_1-value of the pulse, which is approximately 0 for a Gaussian shape. This corresponds to a labelling efficiency of $\alpha_{lab,i} = 0$. Thus, for fast exchange, Ψ_i should be replaced by f_i.

If the changes in the RF envelope are comparable to k_i the state of pool i becomes complicated, however Ψ_i must be somewhere between the upper bound $\Psi_{i,max} = f_i$ and a lower bound given by the value predicted for a block pulse with the same average $\bar{R}_{ex,i}$ which is $\Psi_{i,min} = f_i - \frac{\bar{R}_{ex,i}}{k_i}$. As a first guess, Ψ_i is replaced by $\overline{\Psi}_i = f_i - \frac{\bar{R}_{ex,i}}{k_i}\alpha_{start}$, where α_{start} is introduced as a heuristic parameter ($0 < \alpha_{start} < 1$) that determines $\overline{\Psi}_i$ subject to $\Psi_{i,min} < \overline{\Psi}_i < \Psi_{i,max}$. For the Gaussian pulses employed in the following experiments, the value of $\alpha_{start} = 0.5$ was chosen based on numerical simulations of the Bloch-McConnell equations (see Appendix D).

3. Methods

The convergence of the algorithm and accuracy of determined fit parameters were investigated by fitting the simplified model equations to simulated as well as phantom data for both CW saturation (equation 3) and pulsed saturation (equation 5).

Simulations

Z-spectra were simulated by evaluating the general solution of the BM equations numerically [15] in Matlab (vR2016b). For pulsed saturation, Gaussian-shaped pulses were approximated by piecewise constant pulses, i.e. each pulse was split into 200 uniform segments of constant pulse amplitude.

The simulation parameters describing the sample were chosen to represent typical values of APT phantoms. A two-pool model was assumed with one pool describing the amide proton and the other pool the water proton with the following parameters: $T_{1a} = 3s$, $T_{2a} = 1.5s$,

$T_{1b} = 1s$, $T_{2b} = 0.015s$ and $k_{ba} = 30$Hz. The equilibrium magnetizations were assumed as $M_{0a} = 1$ and $M_{0b} = 0.007$ and the resonance frequency of the amide protons at $\omega_{ba} =$ 3.5ppm. The spectra were sampled at saturation frequency offsets $\Delta\omega_a$ from -6ppm to 6ppm in steps of 0.1ppm. White Gaussian noise with a standard deviation of $\sigma = 0.02$ was added to all simulated spectra before the fitting procedure as we observed this level of noise in Z-spectra of individual 27mm^3 voxels on a 3T clinical scanner, acquired with the snapshot-CEST technique [28]. In order to assess systematic biases and to examine the robustness of the algorithm with either model, each fit was repeated 1000 times with different realizations of this noise. If the algorithms failed to converge to any solution (returning Not-a-Number (NaN) upon encountering operations with undefined numerical results) or rendered negative parameter estimates they were classified as outliers and excluded from the subsequent analysis.

The parameter values of the pulse sequence and MRI scanner assumed for the CW saturation experiment were as follows: $B_0 = 7$T, $B_1 = 3.2\mu$T and pulse duration $t_p = 10$s. The pulsed saturation experiment was simulated with: $B_0 = 7$T, $n = 50$ Gaussian pulses of duration $t_p = 0.1$s, standard deviation $\sigma_p = 0.017s$ and an average amplitude of $B_1 =$ 3.2μT. The duty cycle was $\mathrm{DC} = 0.98$. The means and precisions (defined as the inverses of the variances) of the prior distributions are shown in table 1.

Furthermore, data sets of multiple Z-spectra with varying saturation powers were simulated for CW and pulsed saturation, since the availability of multiple Z-spectra at different B_1 permits the simultaneous estimation of exchange rate and concentration of CEST pools [7,8,11,29,30]. The average amplitudes were $B_1 = 0.5, 1.0, 2.0, 5.0$ and 10.0 μT. All other parameter values were the same as for the single Z-spectra. The assumed prior distributions are shown in table 1.

A further simulation was performed to investigate the performance of the algorithm for Z-spectra with two CEST pools. The simulation parameters were chosen to represent a solution of Taurine and Creatine, whose resonance peaks overlap in our experimentally acquired Z-spectra: $T_{1a} = 3s$, $T_{2a} = 2.2s$, $M_{0b} = 0.00056$, $M_{0c} = 0.0022$, $T_{1b} = T_{1c} = 1s$, $T_{2b} = T_{2c} = 0.015s$, $k_{ba} = 1800\text{Hz}$, $k_{ca} = 80\text{Hz}$, $\omega_{ba} = 3.0\text{ppm}$, $\omega_{ca} = 1.9\text{ppm}$. The spectral sampling and the noise properties were the same as in the previous simulation. Scanner and pulse sequence parameters were: $B_0 = 9.4\text{T}$, $n = 151$, $t_p = 0.1\text{s}$, $\text{DC} = 0.98$ and $\text{B}_1 = 0.78, 1.17, 1.57, 1.96, 2.35, 2.74, 3.13, 3.52, 3.91, 4.31\mu\text{T}$. Using different realizations of the added noise, these fits were repeated 1000 times with the analytical model and due to the long processing time 100 times with the numerical model.

Phantom experiments

For CW saturation experiments a 15mM Iodipamide in phosphate-buffered saline (PBS) solution was measured on a 7T MRI scanner Bruker Avance 300 (Bruker, Ettlingen, Germany), $B_1 = 1.5, 2.0, 3.0$ and $6.0\ \mu\text{T}$ and $t_p = 5\text{s}$. The pH was adjusted to $\text{pH} = 7.4$ and the temperature to $T = 37°\text{C}$. Frequency offsets were between -10ppm and 10ppm in steps of 0.1ppm. The saturation was followed by a fast spin-echo sequence with centric encoding (repetition time TR/echo time TE/number of excitations NEX/RareFactor = 10s/3.5ms/2/64). T_1 relaxation times were measured using a Rapid Acquisition with Relaxation Enhancement (RARE) sequence with eleven repetition times in the range 50-10000ms. T_1 measurements were performed in a central axial plane with the following parameters: TE/NEX/RareFactor =

11ms/3/2, matrix = 128x128, FOV = 30x30mm^2, slice thickness = 3mm, total acquisition time = 1h 7min. Prior distributions assumed for the Bayesian fit are shown in table 3.

To obtain pulsed saturation data, we measured $12.5, 25.0, 50.0 \text{ and } 100.0 \text{ mM}$ Taurine in water solution which consisted of titrated 0.1% PBS with $\text{pH} = 6.2$ and temperature $T = 23°\text{C}$. The data set was acquired on a 9.4T Agilent MRI scanner using a transmit/receive RF coil with 33mm inner diameter (Rapid Biomedical, Germany). The saturation consisted of 151 Gaussian pulses of duration $t_p = 0.05s$, standard deviation $\sigma_p = 0.017$ and duty cycle of DC = 0.98. The average saturation amplitudes were $\text{B}_1 = 0.78, 1.17, 1.57, 1.96, 2.35, 2.74, 3.13, 3.52, 3.91, 4.31 \text{ μT}$. Each spectrum was sampled at 77 equally spaced frequency offsets between −6ppm and 6ppm. The readout sequence was a single-slice 2D-GRE sequence with a field of view of 20 × 20mm^2, matrix size of 64 × 64, TR = 5s, TE = 1.3ms and slice thickness of 4mm. An Inversion recovery EPI sequence was used to quantify T_1. A global adiabatic inversion pulse (flip angle of 180°, duration 2ms) was applied at the frequency of water followed by 20 equally spaced inversion times from 8.1ms to 7.5s. The other parameters were as follows: $TR = 15$s, $TE = 25.5$ms, slice thickness of 2mm, field of view of 20 × 20mm^2 and matrix size of 64 × 64. For the quantification of T_2 the Carr Purcell Meiboom Gill (CPMG) sequence was used. It consisted of a 90° excitation pulse (sinc pulse of 2ms duration) in x-direction followed by 15 refocusing pulses in y-direction (flip angle of 180°, sinc shape and duration of 1.6ms). The other parameters were: TR = 3s, τ_{CPMG} = 8.33ms, slice thickness of 2mm, field of view of 20 × 20mm^2 and matrix size of 64 × 64.

To present an application with 2 CEST agent pools whose peaks overlap in the Z-spectrum, a solution consisting of 0.1% PBS with 25mM Taurine (resonance around 3.0ppm) and 50mM Creatine (resonance around 1.9ppm) was prepared. 5 different levels of acidity (pH = 6.18, 6.44, 6.62, 6.82 7.06) were realized by adding sodium hydroxide (NaOH) and hydrochloric acid (HCl) to the solution. To acquire the Z-spectra the same sequence settings as in the Taurine only experiment were used, but with slightly different saturation amplitudes of $\mathrm{B}_1 = 0.39, 0.78, 1.57, 1.96, 2.35, 2.74, 3.13, 3.52, 3.91, 4.31\ \mu\mathrm{T}$.

For each phantom, mean Z-spectra at various saturation powers were obtained by averaging the measured intensities in a circular region of interest (ROI) covering the phantom vials' cross sections. Additionally, pixel-wise fits were performed on the Taurine data. The Z-spectra were normalized by the average signal of the 5 most negative frequency offsets in order to reduce the impact of noise.

For the implementation of the fitting algorithm the Variational Bayesian (VB) algorithm available in the FMRIB Software Library (v5.0) was used. We extended the model library by replacing the full BM model by the simplified models described by equations 3 and 5. Fits were also performed with the full BM model (according to [11]) to compare the accuracy of parameter estimates and processing times between the two models.

In order to validate the exchange rates determined with the Bayesian fits of the Taurine Z-spectra, a QUESP analysis was performed according to [31] by fitting the full BM equations to the $\mathrm{MTR}_{\mathrm{asym}}$ values at $3.0\mathrm{ppm}$.

4. Results

Simulations

An example of simulated Z-spectra with added Gaussian white noise is shown in figure 1 together with the Bayesian fits obtained with the analytical models. The individual Z-spectra simulated for a single B_1 (figure 1a and 1b) are well described by the fitted spectrum as confirmed in the standard deviation of the fit residuals ($\sigma_{res} = 0.019$ for CW and $\sigma_{res} = 0.029$ for pulsed saturation). Z-spectra simulated at multiple B_1 values (figure 1c and 1d) are also well estimated by the fitted model ($\sigma_{res} = 0.02$), though larger residuals are observable at higher B_1 ($\sigma_{res} = 0.05$), especially close to on-resonance.

Large differences in processing times between analytical and numerical algorithm were observed (table 1). For CW saturation, the algorithm based on the simplified analytical forward model was processed 51 times faster than the numerical forward model when a single B_1 Z-spectrum was fitted and 48 times faster for the fitting of multiple B_1 Z-spectra. For pulsed saturation, the analytical solution led to a 127-fold decrease in processing time for the single Z-spectrum data set and a 108-fold decrease for the multiple B_1 Z-spectra data set.

Repeating these fits 1000 times with different realizations of added white Gaussian noise led to estimated parameter distributions whose means and standard deviations are visualized in figure 2. In the case of CW saturation, no significant biases are observable with respect to the ground truth and standard deviations are comparable between the two algorithms. This is also the case for a single pulsed Z-spectrum except that the numerical model leads to a small underestimation of k_{ba}. In the case of multiple pulsed Z-spectra fitted with either the analytical or the numerical model all estimates are biased, however, the biases when fitting with the numerical model are larger. Outliers, as defined in the methods section, were excluded from the subsequent analysis. Table 1 shows the proportion of converged fits, with the numerical approach generally performing equally well or better than the analytical one.

The equilibrium magnetizations and exchange rates of overlapping CEST pools estimated in the second simulation are visualized in figure 3 (values shown in table 2). With respect to the fast exchanging pool b, both algorithms resulted in underestimations of the equilibrium magnetization of about 10%. The numerical algorithm also led to a similar underestimation of the exchange rate k_{ba}, whereas the analytical algorithm had no significant bias. With respect to the slowly exchanging pool a, the analytical algorithm underestimated the equilibrium magnetization and overestimated the exchange rate by 19.1% and 33.8%, respectively, whereas the numerical algorithm resulted in estimates with no significant biases.

Phantom experiments

The CW saturation Z-spectra of Iodipamide and the corresponding fits obtained with analytical and numerical models are shown in figure 4. The fits were obtained with a fixed relaxation time $T_{1a} = 3.3$s as determined by the Inversion Recovery sequence. The estimated probability distributions for M_{0b}, k_{ba}, ω_b, $\omega_a$and T_{2a} are shown in table 3. Both algorithms led to matching estimates for M_{0b}, k_{ba} and ω_b, but $\Delta\omega_{0,off}$ and T_{2a} are significantly different, i.e. the mean of one estimated distribution is not included in the σ-credible interval of the other estimated distribution.

The averaged Z-spectra of the Taurine phantoms and the corresponding fits are shown in figure 5. The modelled Z-spectra describe the measured data reasonably well and residuals are negligible, except close to on-resonance and at small concentrations. Assuming fixed relaxation times of $T_{1a} = 3.05, 3.04, 3.00, 2.96$s for Taurine concentrations of 12.5, 25.0, 50.0, 100.0mM, respectively, the fit based on the simplified analytical equations yielded the parameter estimates shown in table 4. The estimates for M_{0b} and k_{ba} are plotted against the Taurine concentration in figure 6. Linear relationships were observed in both cases. The exchange rates calculated with the QUESP analysis were: $k_{ba} = 1.05, 2.01, 3.27, 5.58\ k\mathrm{Hz}$ from low to high Taurine concentration. The T_{2a} values estimated by the fit show small differences of the transverse relaxation time of water between the phantoms and larger credible intervals at higher concentration. The increased credible intervals can be explained by a stronger correlation between k_{ba} and T_{2a} at higher concentrations, as both parameters influence the width of the water peak in a similar way. At large exchange rates, as observed in the phantoms with high Taurine concentration, k_{ba} dominates the width of the water peak and makes the estimation of T_{2a} more difficult. On the other hand, when k_{ba} is small, the width of the water peak is dominated by T_{2a}, which can therefore be estimated more accurately. The influence of T_{2b} on the Z-spectra is negligible under the chosen experimental settings, which means that an accurate estimation of this parameter is not possible.

The resulting parameter maps of pixel-wise fits of the Taurine Z-spectra are shown in figure 7. For M_{0a}, M_{0b}, k_{ba}, $\omega_{0,off}$ and $\omega_b$we obtained smooth parameter maps in each phantom, except from a few pixels at the edges of the plastic tubes. In accordance with the fit results of the averaged Z-spectra, k_{ba} and M_{0b} increase with the Taurine concentration. The T_{2a} map is smooth only for the low concentration phantom, but more erroneous estimates were observed the higher the concentration. The parameter maps of M_{0a}, M_{0b}, k_{ba} and ω_b (figure 7 a-d) agree with the fit results obtained from the fit of the averaged Z-spectra. The map of $\Delta\omega_{0,off}$ corresponds to the measured B_0 map and reveals inhomogeneities of up to $\pm 0.15\text{ppm}$. In this way, an additional acquisition of a B_0 map and pre-processing of the Z-spectra can be avoided. The T_{2a} map confirms the interpretation that a large exchange rate reduces the accuracy of the T_{2a} estimation, leading to unrealistic parameter estimates of more than 4s for many pixels.

The averaged Z-spectra with overlapping Creatine and Taurine peaks are shown in figure 8. The parameters M_{0b}, k_{ba}, k_{ca} and $\omega_{0,off}$ were fitted with pool b and c representing the Taurine and Creatine pools, respectively. $T_{1a} = 2.5\text{s}$ was fixed according to the inversion recovery measurement and $T_{2a} = 2.2\text{s}$ was set according to the values estimated in the previous experiment (table 4). The Creatine parameters T_{2c} = 27ms (according to [32]) and $M_{0c} = 0.0018$ were fixed, assuming 4 exchanging protons per Creatine molecule. Furthermore, the Taurine and Creatine peaks were located at $\omega_b = 2.96\text{ppm}$ and $\omega_c = 1.85\text{ppm}$, respectively. The estimated parameters are shown in table 5 and the measured relationship between exchange rates and pH was plotted in figure 9.

Figure 1: Fit results of simulated data sets obtained with the simplified analytical equations for a two-pool model of an amide in water solution: (a) single B_1 CW saturation, (b) single B_1 pulsed saturation, (c) multiple B_1 CW saturation, and (d) multiple B_1 pulsed saturation. The single B_1 Z-spectra were simulated with an average amplitude of $B_1 = 3.2\mu\mathrm{T}$. For multiple B_1 Z-spectra we employed $B_1 = 0.5, 1.0, 2.0, 5.0 \text{ and } 10.0\ \mu\mathrm{T}$. White Gaussian noise was added. Average estimated parameters are shown in table 1.

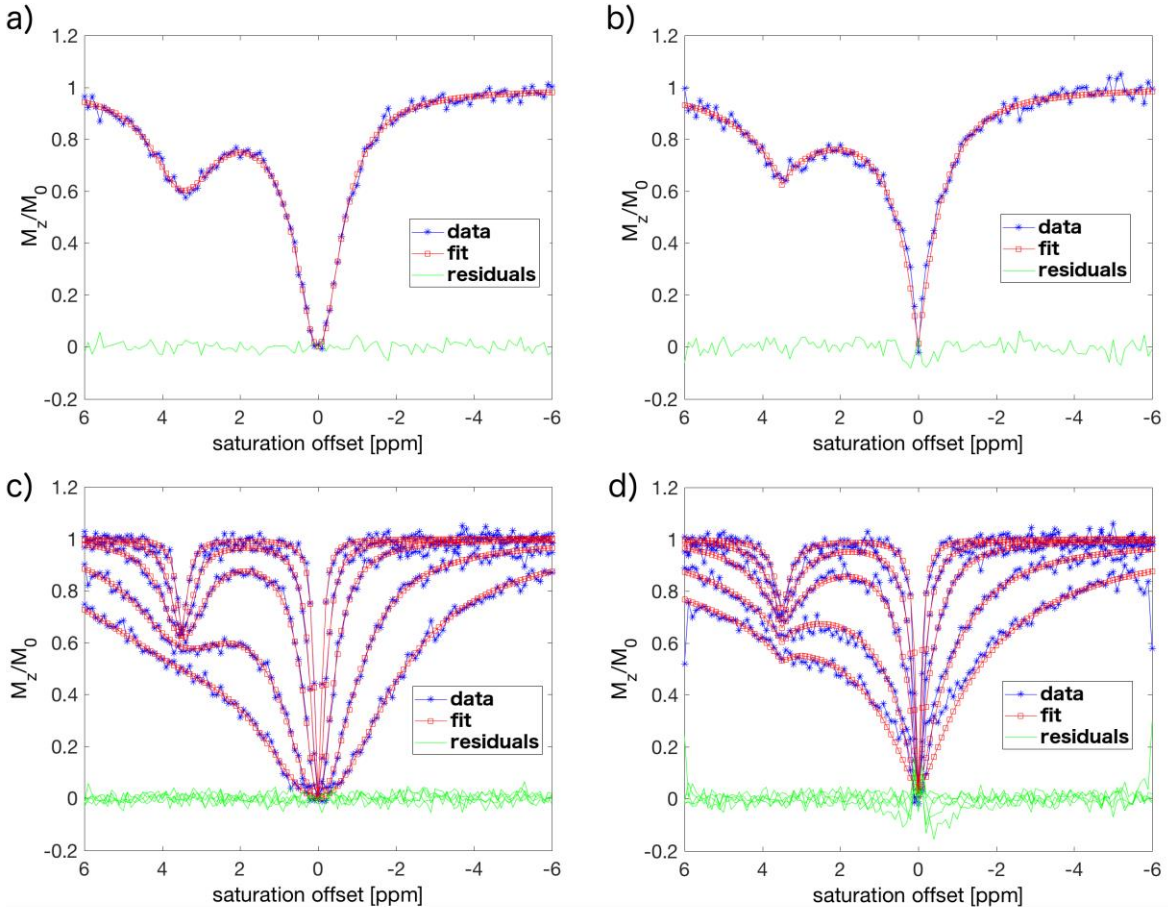

Figure 2: The means and standard deviations of estimated parameter distributions and the CESTR* metric (table 1) obtained from 1000 repetitions of the fitting algorithms. Outliers were removed in the analysis for this figure. Numerical and analytical models were applied to fit simulated Z-spectra with different realizations of white Gaussian noise. The following saturation schemes were investigated: single B_1 CW saturation (sCW), single B_1 pulsed saturation (sP), multiple B_1 CW saturation (mCW), and multiple B_1 pulsed saturation (mP). Note, that M_{0b} was kept fixed for the single B_1 saturation schemes and is therefore only shown for the multiple B_1 saturation schemes.

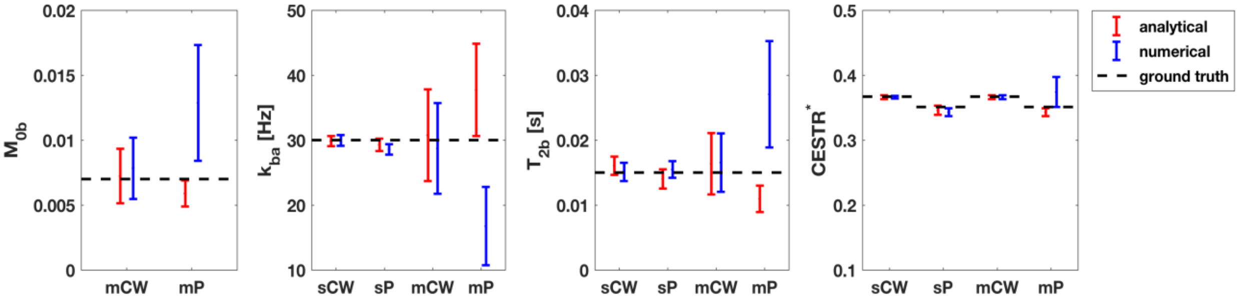

Figure 3: The means and standard deviations of estimated parameter distributions (table 2) obtained from 100 repetitions of the numerical algorithm and 1000 repetitions of the analytical algorithm for pulsed saturation based on simulated Z-spectra with 2 overlapping CEST pools. Each repetition was run with a different realization of white Gaussian noise.

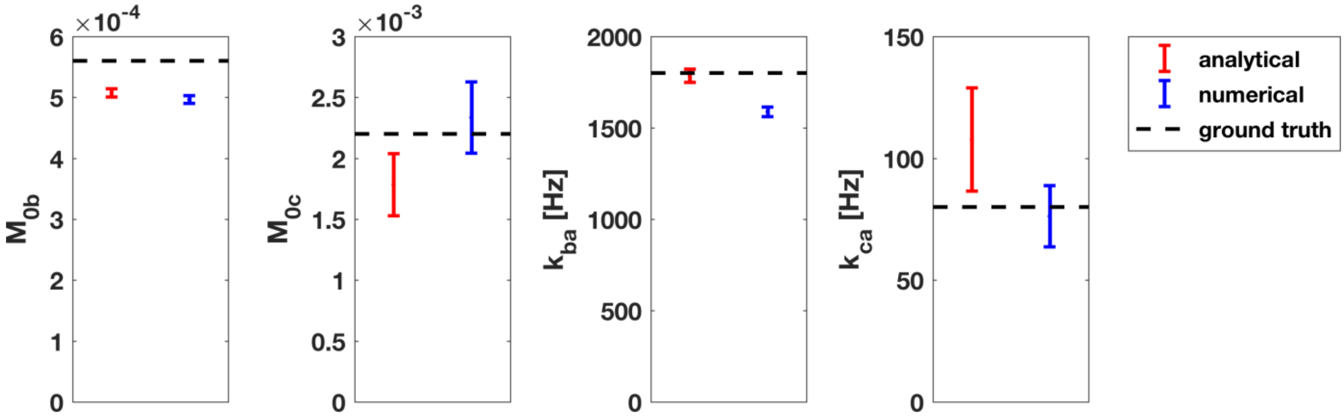

Figure 4: Z-spectra of a 15mM Iodipamide in PBS solution at pH = 7.4 and T = 37°C, acquired at average saturation amplitudes of $B_1 = 1.5, 2.0, 3.0$ and 6.0 μT. The fit was obtained with the simplified analytical equations (a) and the numerical model (b).

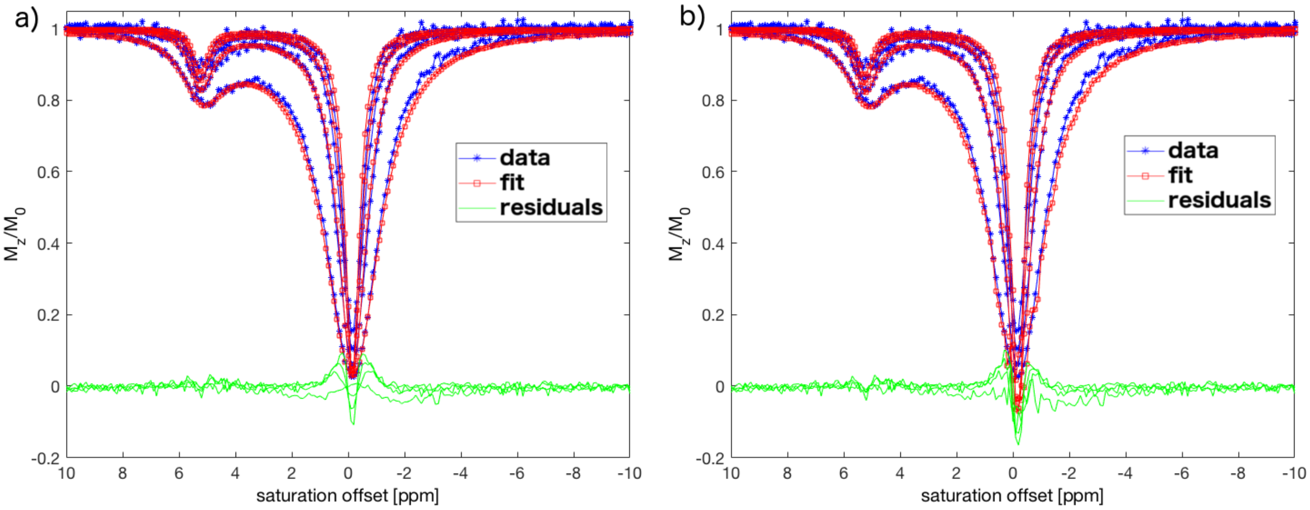

Figure 5: Z-spectra of 12.5mM (a), 25.0mM (b), 50.0mM (c), 100.0mM(d) Taurine in PBS solutions at pH = 6.2 and T = 23°C. The saturation pulse average amplitude was varied with $B_1 = 0.78, 1.17, 1.57, 1.96, 2.35, 2.74, 3.13, 3.52, 3.91, 4.31\ \mu T$. The fits were obtained with the simplified analytical equations for a two-pool model.

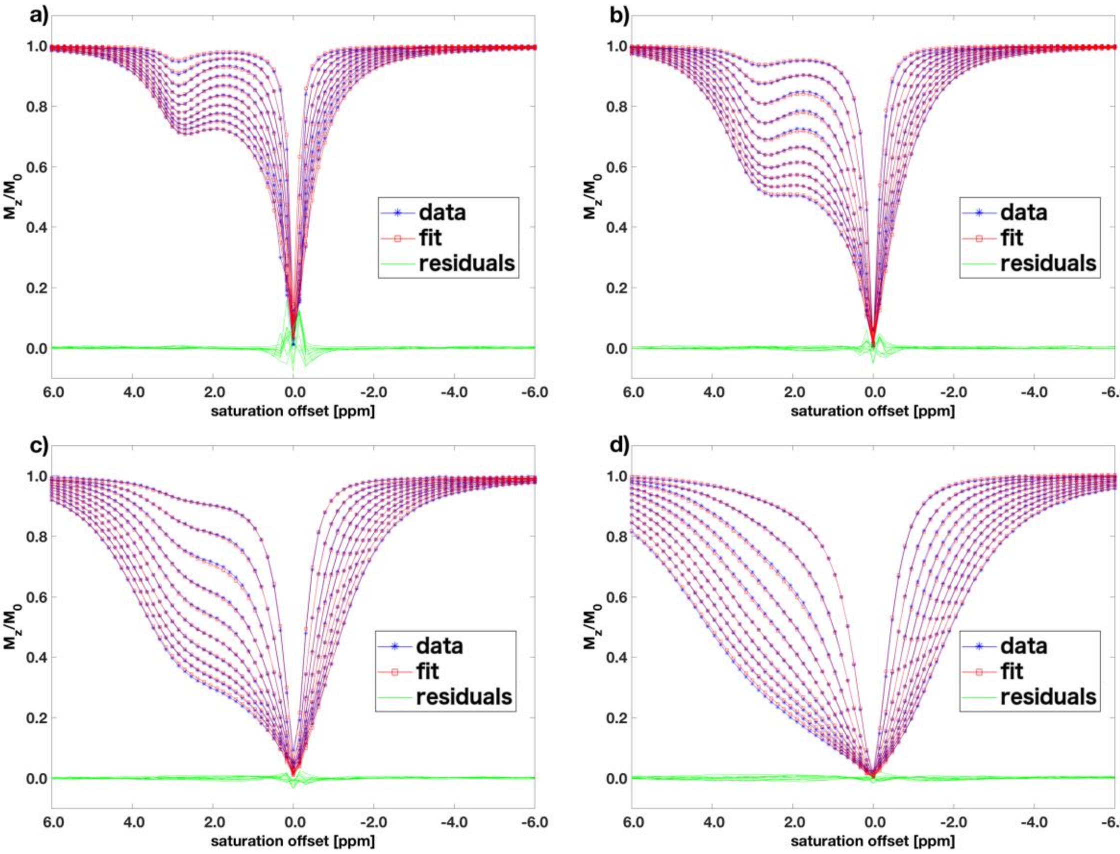

Figure 6: The linear dependencies between Taurine concentration and the means of the distributions of the equilibrium magnetization of the Taurine pool M_{0b} (a) and the exchange rate k_{ba} (b), respectively as estimated by the fit. The error bars in a) correspond to the σ-credible intervals. The linear regression lines are weighted least squares lines where the weights are inverse variances of the estimated parameter distributions. As a comparison, the exchange rates measured with the PRO-QUEST approach in [33] and with the QUESP analysis are shown.

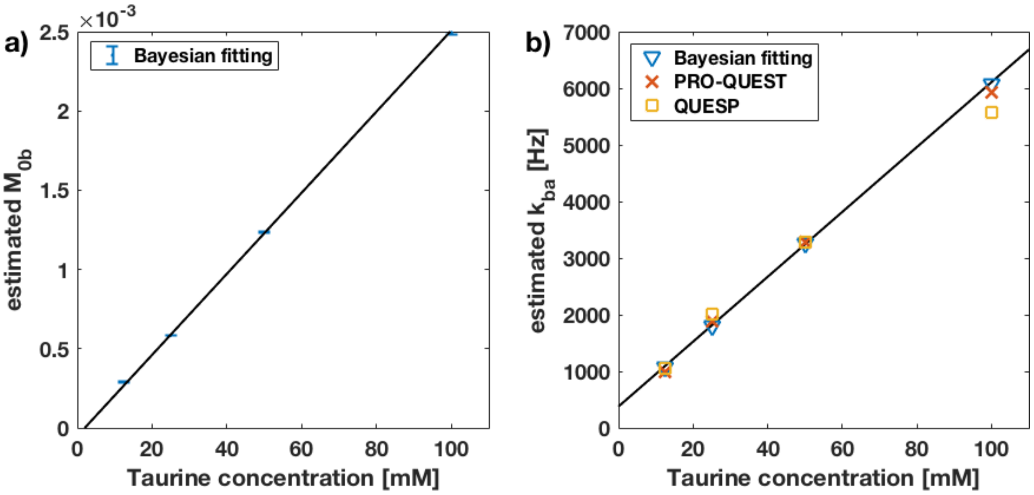

Figure 7: Parameter maps obtained from pixel-wise Bayesian fits of Z-spectra at multiple B_1 of Taurine in PBS solutions at pH = 6.2 and T=23°C a) M_{0a}, b) M_{0b}, c) k_{ba} in Hz, d) $\omega_{0,off}$ in ppm, e) ω_b in ppm, f) T_{2a} in s. The Taurine concentrations from the bottom tube to the top tube are: 12.5mM, 25.0mM, 50.0mM, 100.0mM. The maps were masked to include only those pixels showing the Taurine phantom vials.

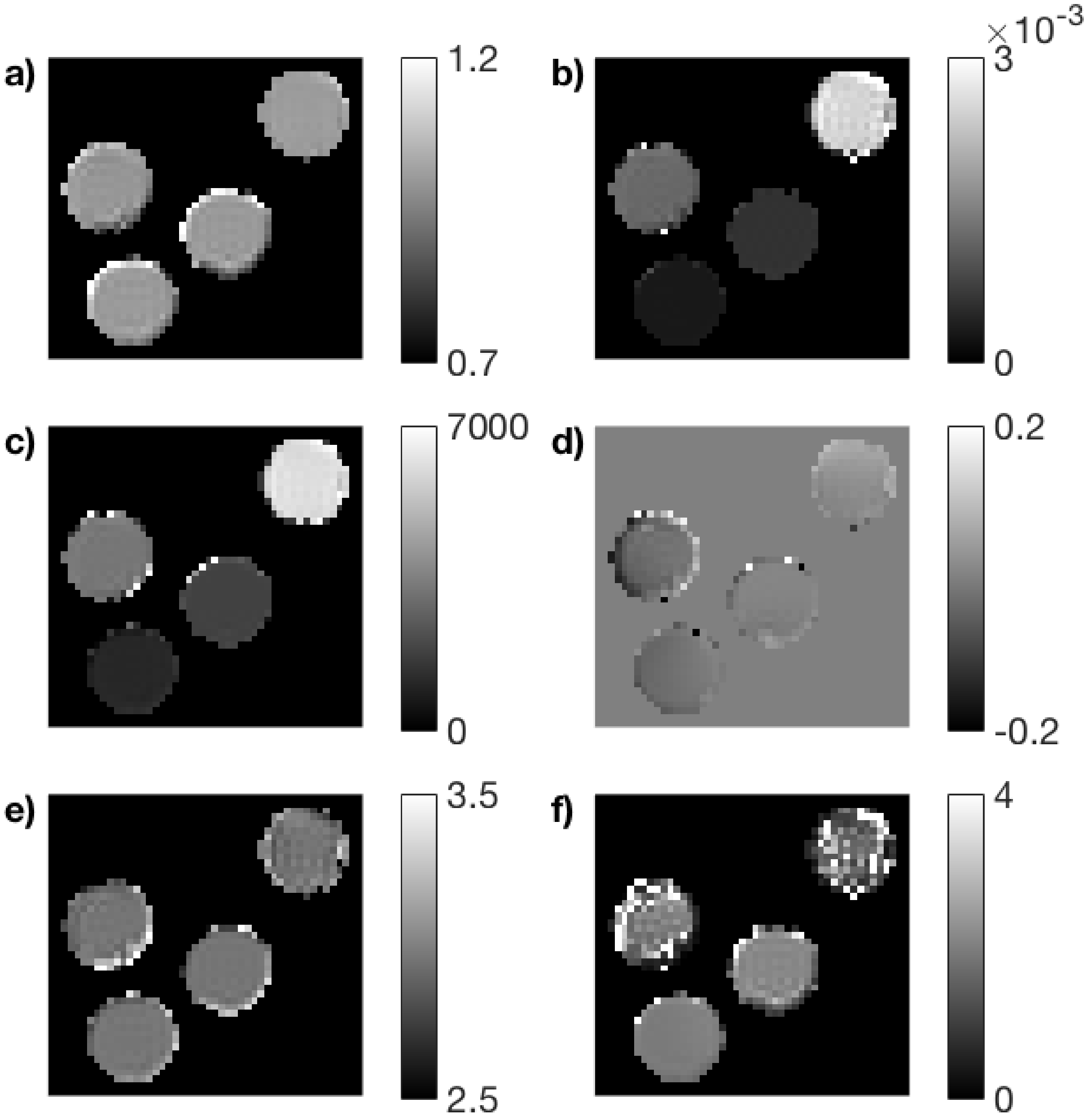

Figure 8: Z-spectra of a 25mM Taurine and 50mM Creatine in PBS solution at T = 20°C and varying acidity: a) pH = 6.18, b) pH = 6.22, c) pH = 6.62, d) pH = 6.82, e) pH = 7.06. The saturation pulse average amplitude was varied with $\mathrm{B}_1 = 0.39, 0.78, 1.57, 1.96, 2.35, 2.74, 3.13, 3.52, 3.91, 4.31\ \mu\mathrm{T}$. The fits were obtained with the simplified analytical equations for a three-pool model.

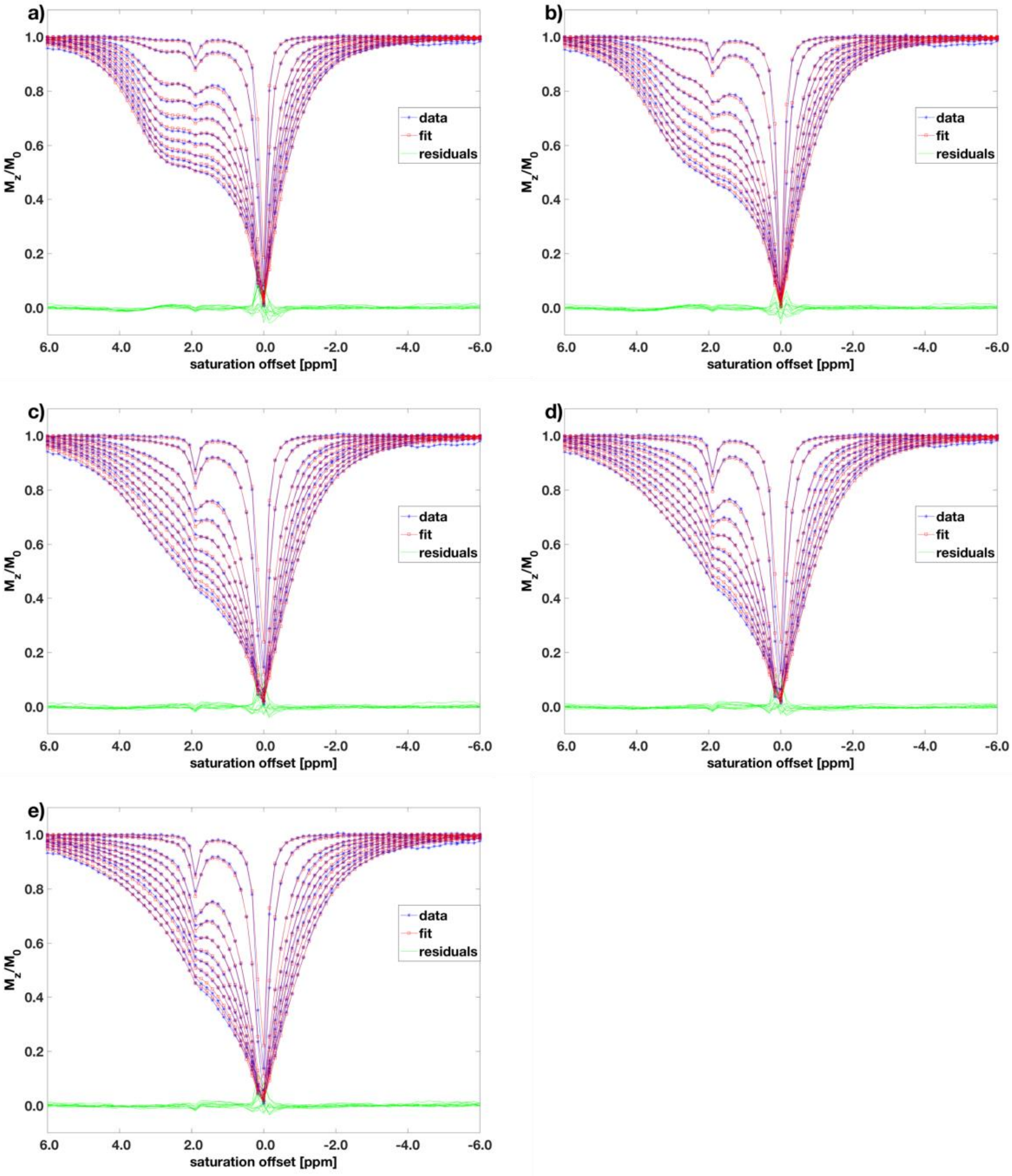

Figure 9: The figures show the estimated exchange rates of a) Taurine and b) Creatine in the same solution, depending on acidity. The values correspond to the estimates obtained from the fits presented in figure 8 and table 5. Two metrics, CESTR* (c) and MTR_{asym} (d) were calculated at the Creatine resonance. CESTR* correlates with the Creatine exchange rate at all saturation amplitudes, whereas MTR_{asym} is skewed by the overlapping Taurine peak, especially at higher saturation amplitudes.

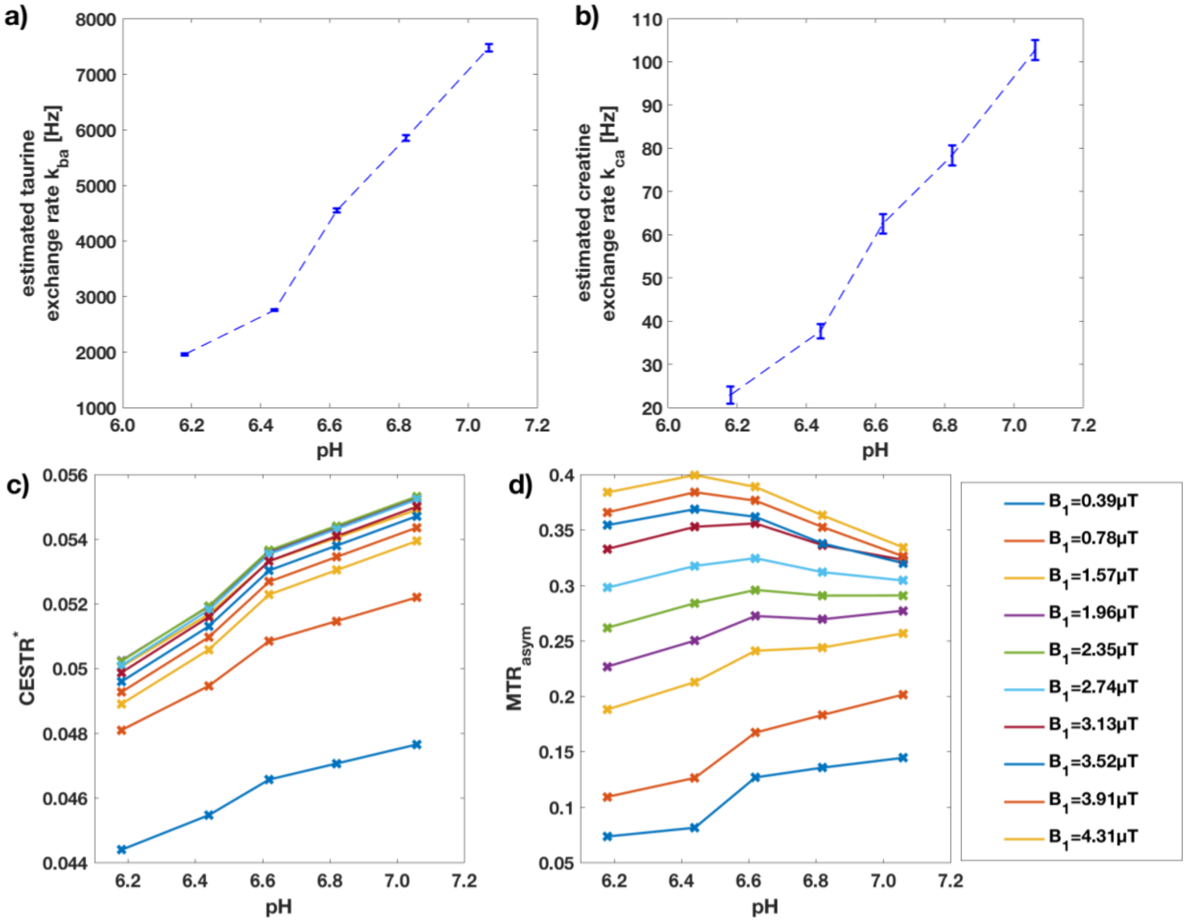

Table 1: Summary of the results obtained from 1000 repetitions of the Bayesian fitting algorithm with numerical and analytical models applied to simulated Z-spectra with a single CEST pool. Each repetition was run with a different realization of white Gaussian noise. The values in brackets correspond to the standard deviation of the estimated means. The error columns contain the relative absolute difference to the ground truth. In addition, the CESTR* values are given for an average saturation amplitude of $B_1 = 3.2\mu\mathrm{T}$. The two values listed under *truth* correspond to the CW case and pulsed case, respectively. The processing times were measured on a 2.9GHz Intel Core i5 processor.

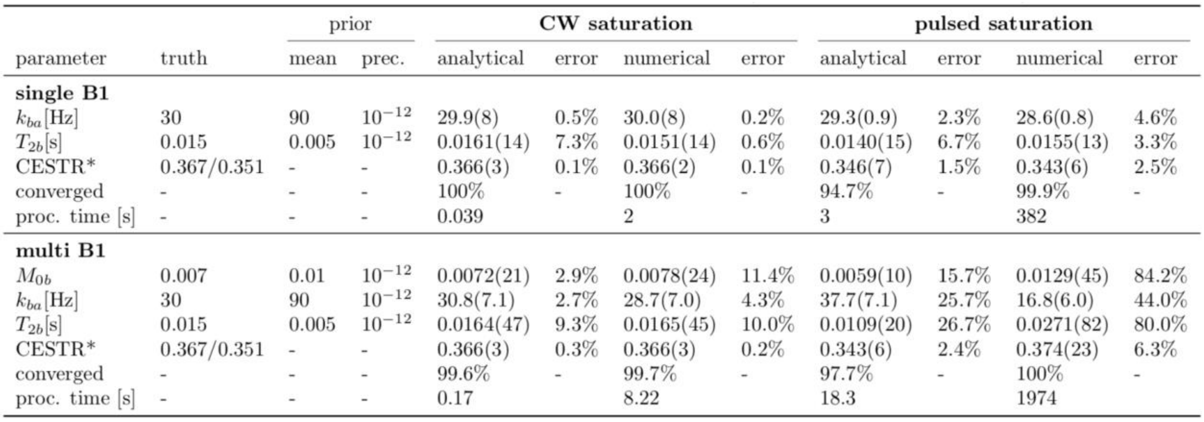

		prior		**CW saturation**				**pulsed saturation**			
parameter	truth	mean	prec.	analytical	error	numerical	error	analytical	error	numerical	error
single B1											
k_{ba}[Hz]	30	90	10^{-12}	29.9(8)	0.5%	30.0(8)	0.2%	29.3(0.9)	2.3%	28.6(0.8)	4.6%
T_{2b}[s]	0.015	0.005	10^{-12}	0.0161(14)	7.3%	0.0151(14)	0.6%	0.0140(15)	6.7%	0.0155(13)	3.3%
CESTR*	0.367/0.351	-	-	0.366(3)	0.1%	0.366(2)	0.1%	0.346(7)	1.5%	0.343(6)	2.5%
converged	-	-	-	100%	-	100%	-	94.7%	-	99.9%	-
proc. time [s]	-	-	-	0.039		2		3		382	
multi B1											
M_{0b}	0.007	0.01	10^{-12}	0.0072(21)	2.9%	0.0078(24)	11.4%	0.0059(10)	15.7%	0.0129(45)	84.2%
k_{ba}[Hz]	30	90	10^{-12}	30.8(7.1)	2.7%	28.7(7.0)	4.3%	37.7(7.1)	25.7%	16.8(6.0)	44.0%
T_{2b}[s]	0.015	0.005	10^{-12}	0.0164(47)	9.3%	0.0165(45)	10.0%	0.0109(20)	26.7%	0.0271(82)	80.0%
CESTR*	0.367/0.351	-	-	0.366(3)	0.3%	0.366(3)	0.2%	0.343(6)	2.4%	0.374(23)	6.3%
converged	-	-	-	99.6%	-	99.7%	-	97.7%	-	100%	-
proc. time [s]	-	-	-	0.17		8.22		18.3		1974	

Table 2: Summary of the results obtained from 1000 repetitions of the fitting algorithm with the analytical model and 100 repetitions with the analytical model applied to simulated Z-spectra with 2 overlapping CEST pools. Each repetition was run with a different realization of white Gaussian noise. The values in brackets correspond to the standard deviation of the estimated means. The error columns contain the relative absolute difference to the ground truth The processing times were measured on a 2.9GHz Intel Core i5 processor.

		prior		**pulsed saturation**			
parameter	truth	mean	prec.	analytical	error	numerical	error
multi B1							
M_{0b}	0.00056	0.0011	10^{-12}	0.00051(1)	8.9%	0.00050(1)	10.7%
M_{0c}	0.0022	0.0044	10^{-12}	0.00178(25)	19.1%	0.00233(29)	6.1%
k_{ba}[Hz]	1800	3600	10^{-12}	1785(35)	0.8%	1588(26)	11.8%
k_{ca}[Hz]	80	160	10^{-12}	107(21)	33.8%	76(12)	5.0%
converged	-	-	-	100%	-	100%	-
proc. time [s]	-	-	-	33		61200	

Table 3: Estimated parameters corresponding to the fits in figure 4 of an Iodipamide solution analysed with the analytical and numerical models. The values correspond to the means of the Gaussian posterior distributions of the estimated parameters. The uncertainty in brackets indicates the standard deviation of these distributions and refers to the last digits of the mean, e.g. $2.63(26) = 2.63 \pm 0.26$.

	prior		estimates (CW)	
parameter	mean	precision	Analytical	Numerical
M_{0b} $[10^{-4}]$	4.00	1.00E-12	2.63(26)	2.87(39)
k_{ba}[Hz]	900	1.00E-12	321(38)	300(47)
$\omega_{0,\mathrm{off}}$[ppm]	0	1.00E-12	-0.153(2)	-0.16720(2)
ω_{b}[ppm]	5.5	1.00E-12	5.42(1)	5.43(2)
$T_{2\mathrm{a}}$[s]	0.211	1.00E-12	1.59(2)	1.81(3)
$T_{2\mathrm{b}}$[s]	10	1.00E-12	10(1000000)	10(1000000)

Table 4: Estimated parameters corresponding to the fits in figure 5 of Taurine solutions at different concentrations, obtained with the analytical model.

parameter	12.5mM	25.0mM	50.0mM	100.0mM
M_{0a} [1]	0.998(1)	0.999(1)	0.994(1)	1.004(1)
M_{0b} $[10^{-4}]$	2.90(6)	5.84(2)	12.34(3)	24.93(12)
$k_{ba}[10^3\mathrm{Hz}]$	1.08(4)	1.79(1)	3.26(4)	6.07(3)
$\omega_{0,\mathrm{off}}$[ppm]	-0.023(1)	0.005(1)	-0.036(1)	0.030(1)
ω_b[ppm]	2.96(1)	2.95(1)	2.95(1)	2.96(1)
$T_{2\mathrm{a}}$[s]	1.96(3)	2.17(3)	2.21(5)	1.74(9)
T_{2b}[s]	20(316)	20(316)	20(316)	20(316)

Table 5: Estimated parameters corresponding to the fits in figure 8 of a Taurine and Creatine solution at varying acidity, obtained with the analytical model.

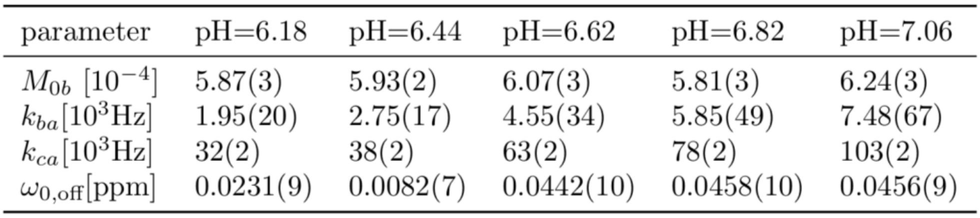

parameter	pH=6.18	pH=6.44	pH=6.62	pH=6.82	pH=7.06
M_{0b} $[10^{-4}]$	5.87(3)	5.93(2)	6.07(3)	5.81(3)	6.24(3)
$k_{ba}[10^3\mathrm{Hz}]$	1.95(20)	2.75(17)	4.55(34)	5.85(49)	7.48(67)
$k_{ca}[10^3\mathrm{Hz}]$	32(2)	38(2)	63(2)	78(2)	103(2)
$\omega_{0,\mathrm{off}}[\mathrm{ppm}]$	0.0231(9)	0.0082(7)	0.0442(10)	0.0458(10)	0.0456(9)

5. Discussion

In this study, a Variational Bayesian algorithm for fast Bayesian inference [13] has been applied to fit CEST data. In contrast to a previous approach based on a general solution of the BM equations [11], we used simplified analytical models with the aim to reduce processing time. To assess the processing times as well as the convergence and accuracy of this evaluation, the algorithm was applied to Z-spectra obtained from simulations as well as phantom experiments under both CW and pulsed saturation. The results show that the simplified algorithm converges to a solution that describes the data well and thus allows us to estimate parameters with an accuracy and precision that is comparable with the previous algorithm.

With this approach, it was however possible to considerably reduce processing time. The approximately 50-fold reduction of computational time for CW saturation can largely be attributed to the reduced complexity of the applied analytical solution. In more details, the numerical solution requires the relatively time-consuming calculation of a matrix exponential, whereas equation 3 comprises only basic arithmetic operations. As the Variational Bayesian algorithm iteratively updates the parameter estimates until convergence, the respective solutions are evaluated for each update.

For pulsed saturation, the reduction of processing time was even greater (up to 127-fold), although the analytical formula for pulsed saturation (equation 5) is more complex than the analytical formula for CW saturation. This significant reduction was possible because the numerical solution requires a separation of the pulse shape into multiple intervals with approximately constant amplitude, each of which requires the numerical evaluation of a matrix exponential. In contrast, with the simplified model the averaging of $R_{1\rho}$ over the pulse shape makes it possible to obtain the parameter update for each iteration with only one evaluation of equation 5.

Assuming the processing times observed in the simulations, the time required for fitting a single slice of 100×100 pixels can be reduced from 5.6 hours to 6.5 minutes in CW saturation. Fitting a slice of these dimensions with pulsed saturation would be infeasible with the numerical solution (~44 days) and would take 8.3 hours with the analytical approximation. Such improvements in processing time might be crucial when quantitative CEST methods are considered for clinical routine. Further reductions on such processing times can be expected by using implementations on computer graphics cards.

The repetition of fits with different instances of added Gaussian white noise allows us to draw conclusions about the accuracy and robustness of the algorithms. The observed biases and standard deviations of the obtained distributions suggest that in most cases the Bayesian algorithm does not yield more accurate results with the numerical model than with the analytical ones. While we attribute the biases of the estimates obtained with the analytical models to the approximating assumptions made in their derivation, particularly the application of effective parameters averaged over the pulse shape, and the choice of the heuristic value α_{start}, no such assumptions are made in the numerical model. Hence, we suspect that the biases observed in the numerical model approach are a result of the algorithm converging towards other local optima in the solution space, which exist due to a strong correlation between the estimated parameters. This interpretation is supported by the observation that the residuals of the numerical approach are always determined by the noise rather than systematic deviations. We expect that the probability of converging towards a particular minimum is dependent on the means of the prior distributions and that therefore the observed biases will vary depending on the choice of these priors. The problem of parameter correlations is inherent in all CEST data and can therefore only be mitigated by different sampling or acquisition techniques. Another approach to this problem offered only by the Bayesian technique is to specify more specific prior distributions, if prior knowledge is available.

In order to fit the Iodipamide Z-spectrum, 6 model parameters were estimated by the analytical and numerical algorithms (table 3). The comparison shows deviations of the posterior distribution which are included in the σ-credible intervals and are therefore not significant for M_{0b}, k_{ba} and ω_b. On the other hand, the differences of $\Delta\omega_{0,off}$ (≈0.014ppm) and T_{2a} (≈ 22ms) don't fall within the credible intervals. As discussed in regard to the deviations in the simulated study, these discrepancies can be explained either by convergence issues (local optima) or by the limited range of validity of the assumptions of the analytical model. The latter is less likely, since equations 3-11 were in good agreement with the numerical solution of the BM equations in [23] for the parameters estimated here. The increased asymmetry of the residuals with respect to the water peak in the numerical solution (figure 4b) suggests that the B_0 correction by estimating $\Delta\omega_{0,off}$ was not successful, resulting in a local optimum and the observed significant biases in $\Delta\omega_{0,off}$ and T_{2a}. The determined relative Iodipamide equilibrium magnetizations (M_{0b}, $= 2.6(3)\cdot 10^{-4}$ and M_{0b}, $= 2.9(4)\cdot 10^{-4}$ for analytical and numerical solutions respectively) are in agreement with the expected value of a 15mM solution, assuming that both Iodipamide and water molecules have 2 exchanging proton sites ($M_{0b} = \frac{15mM \cdot 2protons}{55M \cdot 2protons} \approx 2.7 \cdot 10^{-4}$). The transverse relaxation time of Iodipamide T_{2b} was determined with large uncertainty by both, numerical and analytical algorithm. This is due to the small influence of T_{2b} on the shape of the Z-spectrum. The increased magnitude of residuals close to the water peak was also observed in the simulation experiments and can be attributed to the breakdown of the model assumption of negligible rotation of the water magnetization about the effective magnetic field. This effect becomes more important for shorter pulse duration t_p, higher B_1 and longer T_{2a}. Furthermore, it is also possible that the fixed value for T_{1a} deviates sufficiently from its true value to contribute to the larger residuals at the water peak.

In the Taurine experiment, the linear increase of the measured exchange rate with Taurine concentration was unexpected, since both pH and buffer concentrations were maintained constant. However, an alternative analysis of the same data set with the QUESP method, as well as a different CEST sequence, PRO-QUEST, which was applied to the same phantoms (results published in [33]), confirmed the exchange rates determined by the Bayesian fits. Thus, we conclude that the increase of exchange rates was determined correctly. However, the question by which mechanism the exchange rate is influenced by the Taurine concentration remains open.

One of the major challenges with analysing *in-vivo* Z-spectra is the presence of multiple overlapping peaks. The simulations show that analysing Z-spectra containing a fast exchanging Taurine pool which overlaps with a slowly exchanging Creatine pool using either the analytical or the numerical algorithm can result in biased parameter estimates.

Nevertheless, an expected increase of estimated exchange rates with pH in the Taurine phantom (figure 9a and 9b) can be attributed to a systematic deviation of estimates which maintains the correlation between pH and estimated exchange rates. Additionally, the assumption of a fixed Creatine concentration reduces the uncertainty of the other fit parameters and thus leads to an increased precision. The interpretation of simple metrics such as MTR$_{asym}$ can be difficult for overlapping CEST pools (figure 9c) while CESTR* (more complex metric based on the estimated model parameters) allows for an unbiased interpretation of such data, and correlates with the changes of the Creatine exchange rate (figure 9d).

To date, the Variational Bayesian algorithm on which this study is based [13] is the only Bayesian algorithm that incorporates the BM equations to fit Z-spectra. The main limitation of this study is that the assumptions of the employed analytical solution is valid only for slow and intermediate exchange regimes. Therefore, agents at high pH might yield different estimates due to violation of the assumptions of the analytical solutions. For different exchange regimes, a few publications have reported alternative analytical solutions [8,18–22,34] . Problems related to the correlation between model parameters such as agent concentration and exchange rate are not mitigated by employing improved analytical solutions, as the correlation stems from the data acquisition itself. Instead, improving the sampling strategy can lead to a smaller degree of correlation in the data. An improved sampling strategy can also be advantageous to reduce the measurement time [35] since sampling the full Z-spectrum might not be feasible in a clinical setting.

6. Conclusion

A Bayesian fitting algorithm based on approximate analytical solutions of the BM equations has been employed to fit Z-spectra. A considerable reduction of processing times was observed, while the accuracy of estimated parameters was maintained in both simulation and phantom data. This method is expected to be beneficial for quantification of CEST effects within clinically acceptable data processing time. Therefore, future directions include a wide range of *in vivo* applications utilizing endogenous CEST agent with slow and intermediate exchange regimes, such as patients with cancer or stroke.

7. Acknowledgements

We would like to thank Prof. Dr. M. A. Chappell for providing Matlab scripts to navigate the Variational Bayesian (VB) algorithm for CEST of the FMRIB Software Library. A.K. is supported by the EPSRC-funded UCL Centre for Doctoral Training in Medical Imaging (EP/L016478/1), the Department of Health's NIHR-funded Biomedical Research Centre at University College London Hospitals and by Olea Medical®. The European Union's Horizon 2020 research and innovation programme (Grant Agreement No. 667510, support to M.Z., M.K. D.L. A.A., X.G.) is greatly acknowledged.

Appendix A

For small population fractions ($f_i = \frac{M_{0i}}{M_{0a}} \ll 1$), the parameter $R_{1\rho}$ can be regarded as the rate which is perturbed by chemical exchange. This perturbation can be expressed by the exchange-dependent relaxation rates R_{ex}:

$$R_{1\rho} = R_{eff} + R_{ex}, \tag{13}$$

where R_{ex} is comprised of the contributions from each CEST agent pool i:

$$R_{ex} = \sum_i R_{ex,i}, \tag{14}$$

R_{eff} is the unperturbed relaxation rate in the rotating frame, i.e. without exchange, which can be approximated by [36]:

$$R_{eff} = \cos^2(\theta)\, R_{1a} + \sin^2(\theta)\, R_{2a}. \tag{15}$$

The following assumptions are made to obtain a simplified expression for $R_{ex,i}$:

1. The influence of R_{1a} and R_{2a} on $R_{ex,i}$ is negligible,
2. $R_{1i} \ll R_{1a}$ and $R_{1i} \ll k_{ia}$,
3. R_{ex} can be linearized in k_{ai}.

Under these assumptions, R_{ex} can be approximated by:

$$R_{ex,i} = \frac{R_{ex}^{max}\frac{\Gamma^2}{4}}{\frac{\Gamma^2}{4} + \Delta\omega_i^2} \tag{16}$$

with

$$R_{ex,i}^{max} = f_i k_{ia} \sin^2(\theta) \frac{(\omega_i - \omega_a)^2 + \frac{R_{2i}}{k_{ia}}(\omega_1^2 + \Delta\omega^2) + R_{2i}(k_{ia} + R_{2i})}{\frac{\Gamma_i^2}{4}} \tag{17}$$

and

$$\Gamma_i = 2\sqrt{\frac{k_{ia}+R_{2i}}{k_{ia}}\omega_1^2 + (k_{ia} + R_{2i})^2}. \tag{18}$$

Here, $\Delta\omega_i = \omega_{rf} - \omega_i$ is the difference between the frequency of the CW irradiation and the resonance frequency of pool i.

Appendix B

Here, approximations towards a model for pulsed saturation with rectangular pulses of duration t_p, interleaved with delays of duration t_d as published in Appendix A of [21] for two pools are presented for multiple pools.

The operators H_{pulse} and H_{pause} describe the evolution of the water pool magnetization during the RF pulse and during the delay, respectively.

The assumption is that during the pulse the magnetization $Z(t)$ decays with relaxation rate $R_{1\rho}$ (equation 13) towards the steady state $Z_{\text{CW}}^{\text{SS}}$ as described by equation 3:

$$Z(t_p) = H_{\text{pulse}}[Z(t=0)] = (P_z P_{zeff} Z(t=0) - Z_{\text{CW}}^{\text{SS}})\exp(-\mathrm{R}_{1\rho} t_p) + Z_{\text{CW}}^{\text{SS}}. \tag{19}$$

Assuming a multi-exponential recovery of pool a during the pause with one exponential component per pool, and furthermore assuming negligible magnetization exchange between any two CEST agent pools, the evolution of the water pool z-magnetization is given by:

$$Z(t_d) = H_{\text{pause}}[Z(t=0)] = d_{aa}(Z(t=0)-1) + \textstyle\sum_i (d_{ai}\Psi_i Z(t=0) - f_i) + 1. \tag{20}$$

Note, that the only difference compared to equation A2 in [21] is the summation over all CEST agent pools i.

The combined effect of the delay and the pulse is thus expressed by:

$$\begin{aligned} Z(t_p+t_d) &= H_{\text{pulse}}\{H_{\text{pause}}[Z(t=0)]\} \\ &= \underbrace{P_z P_{zeff}\left(d_{aa} + \sum_i (d_{ai}\,\Psi_i)\right)\exp(-\mathrm{R}_{1\rho} t_p)}_{\beta} Z(t=0) \\ &\quad + \underbrace{P_z P_{zeff}\left(1 - d_{aa} - \sum_i (f_i d_{ai})\right)\exp(-\mathrm{R}_{1\rho} t_p) + Z_{\text{CW}}^{\text{SS}}(1-\exp(-\mathrm{R}_{1\rho} t_p))}_{\alpha} \end{aligned} \tag{21}$$

Since the magnetization at the end of this pause-pulse module corresponds to the initial magnetization of the consecutive pause-pulse module, one can formulate the following recursive relationship for the magnetization after n pause-pulse modules:

$$Z(n) = \beta Z(n-1) + \alpha \tag{22}$$

Using the formula for the geometrical series, this relationship is simplified as:

$$Z(n) = \beta^n \left(Z(t=0) - \frac{\alpha}{1-\gamma}\right) + \frac{\alpha}{1-\gamma}. \tag{23}$$

By interpreting $Z_{\mathrm{pulsed}}^{\mathrm{SS}} = \frac{\alpha}{1-\gamma}$ as the steady-state magnetization and defining $Z_{\mathrm{i}} = Z(t=0)$, one obtains equation 5.

Appendix C

Expressions for d_{aa} and d_{ab} were presented in [37], as part of the biexponential solution of the BM equations for $B_1 = 0$ (no saturation) and negligible transverse magnetization ($M_{\mathrm{i}x} = M_{\mathrm{i}y} = 0$):

$$d_{aa} = \frac{(\lambda_1 + R_{1b} + k_{ba})\exp(\lambda_1 t_d) - (\lambda_2 + R_{1b} + k_{ba})\exp(\lambda_2 t_d)}{\lambda_1 - \lambda_2} \tag{24}$$

$$d_{ab} = \frac{k_{ba}(\exp(\lambda_1 t_d) - \exp(\lambda_2 t_d))}{\lambda_1 - \lambda_2} \tag{25}$$

Expressions for λ_1 and λ_2 are:

$$\begin{aligned}\lambda_1 = -\frac{1}{2}\Big(&k_{ab} + k_{ba} + R_{1a} + R_{1b} \\ &+ \sqrt{(k_{ab} + k_{ba} + R_{1a} + R_{1b})^2 - 4(k_{ba}R_{1a} + k_{ab}R_{1b} + R_{1a}R_{1b})}\Big)\end{aligned} \tag{26}$$

$$\lambda_2 = -\frac{1}{2}\Big(k_{ab} + k_{ba} + R_{1a} + R_{1b} - \sqrt{(k_{ab} + k_{ba} + R_{1a} + R_{1b})^2 - 4(k_{ba}R_{1a} + k_{ab}R_{1b} + R_{1a}R_{1b})}\Big) \tag{27}$$

The following terms that appear in equations 6 and 7 can be approximated for $k_{ba} \gg R_{1a}$:

$$d_{aa} + f_b d_{ab} \approx \exp(-R_{1a}t_d) \tag{28}$$

$$d_{aa} + \Psi d_{ab} \approx \exp(-R_{1a}t_d)(1 - \alpha_{lab,b} f_b) \tag{29}$$

For multiple CEST agent pools we apply the corresponding approximations for $k_{ia} \gg R_{1a}$:

$$d_{aa} + \sum_i f_i d_{ai} \approx \exp(-R_{1a}t_d) \tag{30}$$

$$d_{aa} + \sum_i \Psi_i d_{ai} \approx \exp(-R_{1a}t_d)(1 - \sum_i \alpha_{lab,i} f_i) \tag{31}$$

Appendix D

Figure 10 shows the dependence of the numerically determined ideal value of α_{start} on the exchange rate k_{ia} and the average pulse amplitude B_1. For large k_{ia}, α_{start} should be chosen close to 1, whereas $\alpha_{start} = 0$ is a good choice for small k_{ia}. In the intermediate regime of amide exchange rates, a value of $\alpha_{start} \approx 0.5$ is a reasonable choice. In figure 11 the effect of this choice of α_{start} on the analytical solution is shown for different saturation powers and assuming an exchange rate of $k_{ia} = 30\text{Hz}$. Note that the analytical solution is closer to the numerical solution for $\alpha_{start} = 0.5$ than for $\alpha_{start} = 0$ or $\alpha_{start} = 1$. For faster exchange rates the influence of α_{start} on the Z-spectrum is negligible (Figure 12). Hence, $\alpha_{start} = 0.5$ was chosen for all fits in this study.

Figure 10: Dependence of the ideal value of α_{start} on the exchange rate and the average saturation amplitude. The value was calculated according to $\alpha_{start} = \frac{\Psi_{max}-\Psi}{\Psi_{max}-\Psi_{\min}}$, where $\Psi = \frac{M_{zb}(t=t_p)}{M_{za}(t=t_p)}$ was calculated by solving the 2-pool BM equations numerically. The simulation parameters were the same as those of the simulation experiment described in the Methods section.

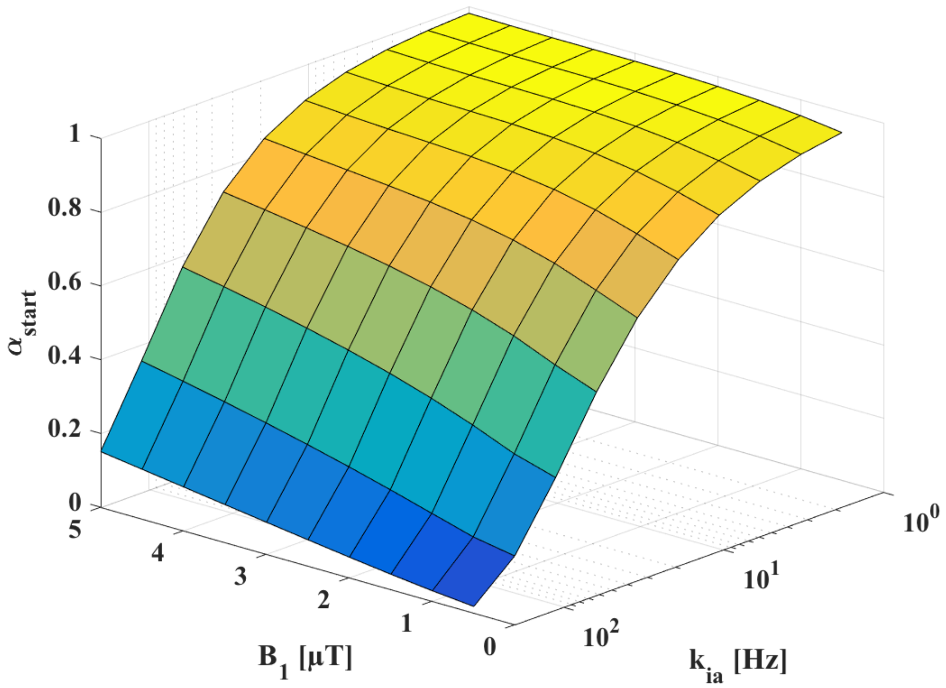

Figure 11: Comparison of the effect of different values of α_{start} on the analytical solution for pulsed saturation with Gaussian pulses at different average saturation amplitudes. The left column shows full Z-spectra and the right column shows a magnification of the solute peak. The simulation parameters were the same as those of the simulation experiment described in the Methods chapter, in particular $k_{ba} = 30$Hz. At this exchange rate, $\alpha_{start} = 0.5$ is a reasonable choice.

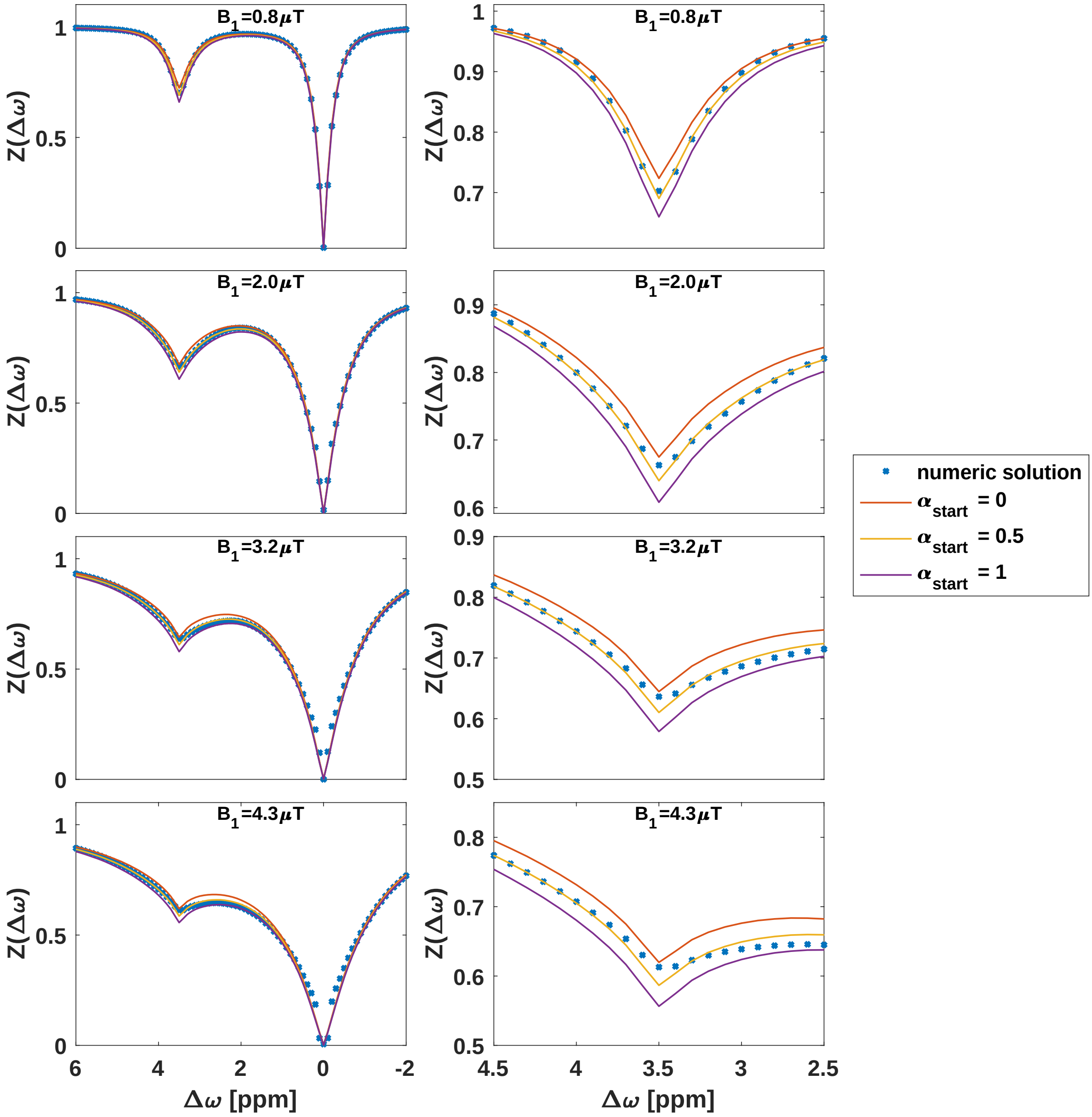

Figure 12: Comparison of the effect of different values of α_{start} on the analytical solution for pulsed saturation with Gaussian pulses at different average saturation amplitudes. Regarding the simulation parameters, the only difference to Figure 11 is the exchange rate which was increased to $k_{ba} = 300$Hz. The figure shows that at faster exchange rates, the influence of α_{start} on the analytical Z-spectrum is negligible. Note, that the analytical Z-spectra overlap and are therefore almost not distinguishable.

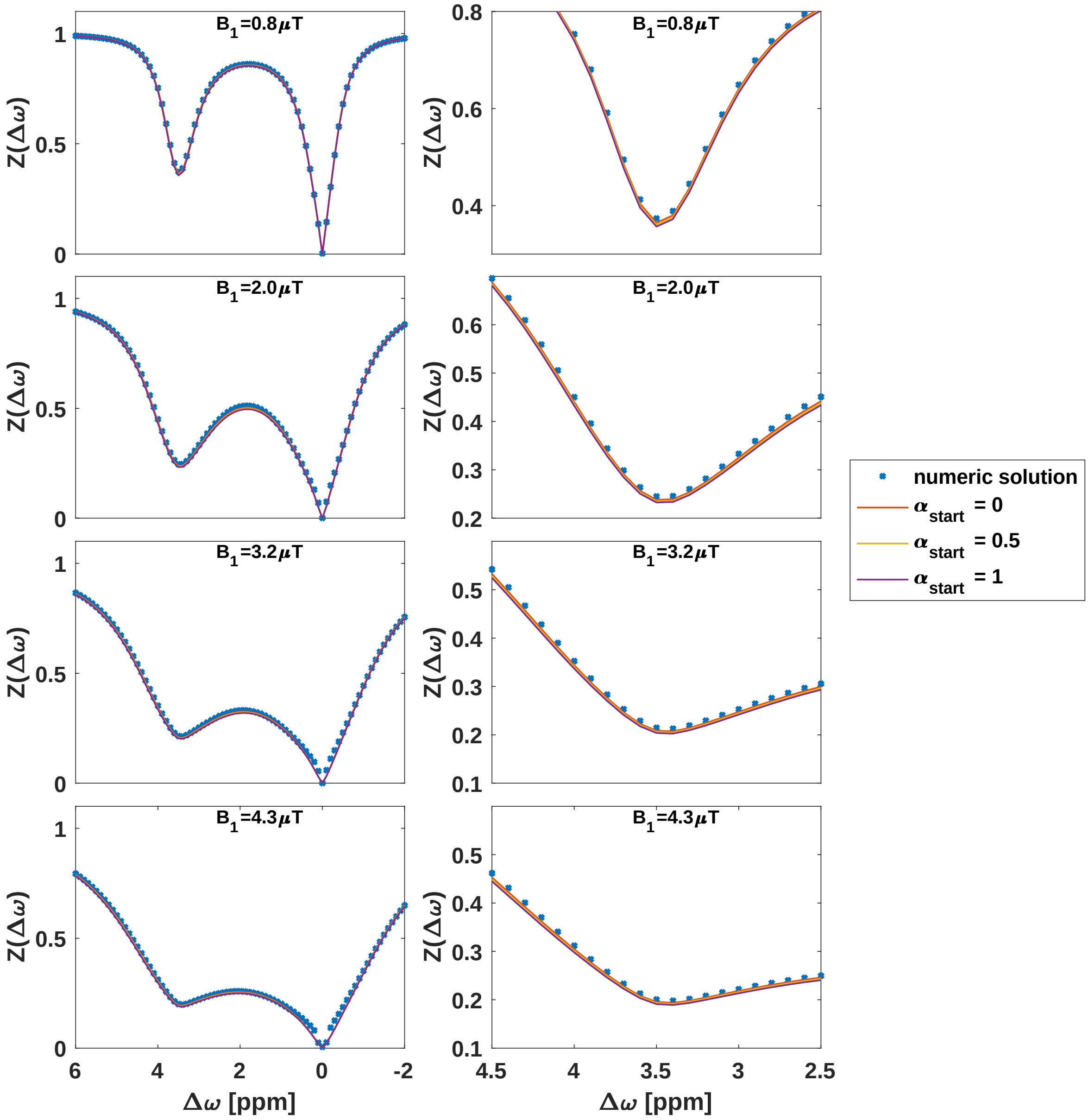

8. References

1. Ward K., Aletras A., Balaban R. A New Class of Contrast Agents for MRI Based on Proton Chemical Exchange Dependent Saturation Transfer (CEST). Journal of Magnetic Resonance. 2000;143(1):79–87. doi:10.1006/jmre.1999.1956

2. Van Zijl PCM, Yadav NN. Chemical exchange saturation transfer (CEST): What is in a name and what isn't? Magnetic Resonance in Medicine. 2011;65(4):927–948. doi:10.1002/mrm.22761

3. Longo DL, Cutrin JC, Michelotti F, Irrera P, Aime S. Noninvasive evaluation of renal pH homeostasis after ischemia reperfusion injury by CEST-MRI. NMR in Biomedicine. 2017;30(7):e3720. doi:10.1002/nbm.3720

4. Longo DL, Bartoli A, Consolino L, Bardini P, Arena F, Schwaiger M, Aime S. In vivo imaging of tumor metabolism and acidosis by combining PET and MRI-CEST pH imaging. Cancer Research. 2016;76(22):6463–6470. doi:10.1158/0008-5472.CAN-16-0825

5. Tietze A, Blicher J, Mikkelsen IK, Østergaard L, Strother MK, Smith SA, Donahue MJ. Assessment of ischemic penumbra in patients with hyperacute stroke using amide proton transfer (APT) chemical exchange saturation transfer (CEST) MRI. NMR in Biomedicine. 2014;27(2):163–174. doi:10.1002/nbm.3048

6. Sun PZ, Wang Y, Dai ZZ, Xiao G, Wu R. Quantitative chemical exchange saturation transfer (qCEST) MRI - RF spillover effect-corrected omega plot for simultaneous determination of labile proton fraction ratio and exchange rate. Contrast Media and Molecular Imaging. 2014;9(4):268–275. doi:10.1002/cmmi.1569

7. Dixon WT, Ren J, Lubag AJM, Ratnakar J, Vinogradov E, Hancu I, Lenkinski RE, Sherry AD. A

concentration-independent method to measure exchange rates in PARACEST agents. Magnetic Resonance in Medicine. 2010;63(3):625–632. doi:10.1002/mrm.22242

8. McMahon MT, Gilad AA, Zhou J, Sun PZ, Bulte JWM, Van Zijl PCM. Quantifying exchange rates in chemical exchange saturation transfer agents using the saturation time and saturation power dependencies of the magnetization transfer effect on the magnetic resonance imaging signal (QUEST and QUESP): pH calibration for poly. Magnetic Resonance in Medicine. 2006;55(4):836–847. doi:10.1002/mrm.20818

9. Sun PZ. Simplified quantification of labile proton concentration-weighted chemical exchange rate (k ws) with RF saturation time dependent ratiometric analysis (QUESTRA): Normalization of relaxation and RF irradiation spillover effects for improved quantitative ch. Magnetic Resonance in Medicine. 2012;67(4):936–942. doi:10.1002/mrm.23068

10. Jones CK, Huang A, Xu J, Edden RAE, Schär M, Hua J, Oskolkov N, Zacà D, Zhou J, McMahon MT, et al. Nuclear Overhauser enhancement (NOE) imaging in the human brain at 7T. NeuroImage. 2013;77:114–124. doi:10.1016/j.neuroimage.2013.03.047

11. Chappell MA, Donahue MJ, Tee YK, Khrapitchev AA, Sibson NR, Jezzard P, Payne SJ. Quantitative Bayesian model-based analysis of amide proton transfer MRI. Magnetic Resonance in Medicine. 2013;70(2):556–567. doi:10.1002/mrm.24474

12. Ray KJ, Larkin JR, Tee YK, Khrapitchev AA, Karunanithy G, Barber M, Baldwin AJ, Chappell MA, Sibson NR. Determination of an optimally sensitive and specific chemical exchange saturation transfer MRI quantification metric in relevant biological phantoms. NMR in Biomedicine. 2016;29(11):1624–1633. doi:10.1002/nbm.3614

13. Chappell MA, Groves AR, Whitcher B, Woolrich MW. Variational Bayesian inference for a nonlinear forward model. IEEE Transactions on Signal Processing. 2009;57(1):223–236. doi:10.1109/TSP.2008.2005752

14. Woessner DE, Zhang S, Merritt ME, Sherry AD. Numerical solution of the Bloch equations provides insights into the optimum design of PARACEST agents for MRI. Magnetic Resonance in Medicine. 2005;53(4):790–799. doi:10.1002/mrm.20408

15. Murase K, Tanki N. Numerical solutions to the time-dependent Bloch equations revisited. Magnetic Resonance Imaging. 2011;29(1):126–131. doi:10.1016/j.mri.2010.07.003

16. Bloch F. Nuclear induction. Physical Review. 1946;70(7–8):460–474. doi:10.1103/PhysRev.70.460

17. McConnell HM. Reaction Rates by Nuclear Magnetic Resonance. The Journal of Chemical Physics. 1958;28(3):430–431. doi:10.1063/1.1744152

18. Zhou J, Zijl PCM van. Chemical exchange saturation transfer imaging and spectroscopy. Progress in Nuclear Magnetic Resonance Spectroscopy. 2006;48(2–3):109–136. doi:10.1016/j.pnmrs.2006.01.001

19. Sun PZ, Murata Y, Lu J, Wang X, Lo EH, Sorensen AG. Relaxation-compensated fast multislice amide proton transfer (APT) imaging of acute ischemic stroke. Magnetic Resonance in Medicine. 2008;59(5):1175–1182. doi:10.1002/mrm.21591

20. Zaiss M, Bachert P. Chemical exchange saturation transfer (CEST) and MR Z-spectroscopy in vivo: a review of theoretical approaches and methods. Phys. Med. Biol. 2013;58:221–269. doi:10.1088/0031-9155/58/22/R221

21. Roeloffs V, Meyer C, Bachert P, Zaiss M. Towards quantification of pulsed spinlock and CEST at clinical MR scanners : an analytical interleaved saturation – relaxation (ISAR) approach. NMR in Biomedicine. 2015;28(October 2014):40–53. doi:10.1002/nbm.3192

22. Gochberg DF, Does MD, Zu Z, Lankford CL. Towards an analytic solution for pulsed CEST. NMR in Biomedicine. 2018 May;31(5):e3903. doi:10.1002/nbm.3903

23. Zaiss M, Bachert P. Exchange-dependent relaxation in the rotating frame for slow and

intermediate exchange - modeling off-resonant spin-lock and chemical exchange saturation transfer. NMR in Biomedicine. 2013;26(5):507–518. doi:10.1002/nbm.2887

24. Roell SA, Dreher W, Leibfritz D. A general solution of the standard magnetization transfer model. Journal of Magnetic Resonance. 1998;132(1):96–101. doi:10.1006/JMRE.1998.1393

25. Michaeli S, Sorce DJ, Springer CS, Ugurbil K, Garwood M. T1ρMRI contrast in the human brain: Modulation of the longitudinal rotating frame relaxation shutter-speed during an adiabatic RF pulse. Journal of Magnetic Resonance. 2006;181(1):135–147. doi:10.1016/j.jmr.2006.04.002

26. Mangia S, Liimatainen T, Garwood M, Michaeli S. Rotating frame relaxation during adiabatic pulses vs. conventional spin lock: simulations and experimental results at 4 T. Magnetic Resonance Imaging. 2009;27(8):1074–1087. doi:10.1016/j.mri.2009.05.023

27. Zu Z, Janve VA, Xu J, Does MD, Gore JC, Gochberg DF. A new method for detecting exchanging amide protons using chemical exchange rotation transfer. Magnetic Resonance in Medicine. 2013;69(3):637–647. doi:10.1002/mrm.24284

28. Zaiss M, Ehses P, Scheffler K. Snapshot-CEST: Optimizing spiral-centric-reordered gradient echo acquisition for fast and robust 3D CEST MRI at 9.4 T. NMR in Biomedicine. 2018;31(4):e3879. doi:10.1002/nbm.3879

29. Desmond KL, Stanisz GJ. Understanding quantitative pulsed CEST in the presence of MT. Magnetic Resonance in Medicine. 2012;67(4):979–990. doi:10.1002/mrm.23074

30. Sun PZ. Simultaneous determination of labile proton concentration and exchange rate utilizing optimal RF power: Radio frequency power (RFP) dependence of chemical exchange saturation transfer (CEST) MRI. Journal of magnetic resonance (San Diego, Calif. : 1997). 2010;202(2):155–61. doi:10.1016/j.jmr.2009.10.012

31. Zaiss M, Angelovski G, Demetriou E, Mcmahon MT, Golay X, Scheffler K. QUESP and QUEST revisited - fast and accurate quantitative CEST experiments. Magnetic Resonance in Medicine. 2017 Jul 7. doi:10.1002/mrm.26813

32. Pankowska A, Kochalska K, Orzylowska A, Lazorczyk A, Wojtowicz A, Dyndor K, Pietura R, Rola R, Stanisz G. Molecular imaging of depression-related brain metabolites using CEST technique -phantom study. In: European Congress of Radiology. 2018. doi:10.1594/ecr2018/C-1521

33. Demetriou E, Tachrount M, Zaiss M, Shmueli K, Golay X. PRO-QUEST: An effective and rapid method for exchange rate quantification based on PROgressive saturation for Quantifying Exchange using Saturation Times in Chemical Exchange Saturation Transfer (CEST). 2017.

34. Davis DG, Perlman ME, London RE. Direct Measurements of the Dissociation-Rate Constant for Inhibitor-Enzyme Complexes via the T1ρand T2(CPMG) Methods. Journal of Magnetic Resonance, Series B. 1994;104(3):266–275. doi:10.1006/jmrb.1994.1084

35. Tee YK, Khrapitchev AA, Sibson NR, Payne SJ, Chappell MA. Optimal sampling schedule for chemical exchange saturation transfer. Magnetic Resonance in Medicine. 2013;70(5):1251–1262. doi:10.1002/mrm.24567

36. Trott O, Palmer AG. Theoretical study of R1(rho) rotating-frame and R2 free-precession relaxation in the presence of n-site chemical exchange. Journal of Magnetic Resonance. 2004;170(1):104–112. doi:10.1016/j.jmr.2004.06.005

37. Zhou J, Wilson DA, Sun PZ, Klaus JA, van Zijl PCM. Quantitative description of proton exchange processes between water and endogenous and exogenous agents for WEX, CEST, and APT experiments. Magnetic Resonance in Medicine. 2004;51(5):945–952. doi:10.1002/mrm.20048